Study of the Cytotoxic Effect of Au@Rh Core-Shell Metal Particles on the Osteosarcoma Cell Line HOS and the hFOB Osteoblast Cell Line

Sergio Zamudio-Lucero , Martín Daniel Trejo-Valdez * , Nury Pérez-Hernández , Ángel Bañuelos-Hernández , María Elena Manríquez-Ramírez

Posted Date: 20 April 2026

doi: 10.20944/preprints202604.1292.v1

Keywords: core-shell nanoparticles; cytotoxicity; osteosarcoma cells

 doi:10.20944/preprints202604.1292.v1

Article

Study of the Cytotoxic Effect of Au@Rh Core-Shell Metal Particles on the Osteosarcoma Cell Line HOS and the hFOB Osteoblast Cell Line

Sergio Zamudio-Lucero [1,2,3], Martín Trejo-Valdez [2,*], Nury Pérez-Hernández [3], Ángel Bañuelos-Hernández [3] and María Elena Manríquez-Ramírez [2]

[1] Unidad Profesional Interdisciplinaria de Biotecnología (UPIBI), Instituto Politécnico Nacional (IPN). Av. Acueducto, La Laguna Ticomán, Gustavo A. Madero, 07340 Ciudad de México, México

[2] Escuela Superior de Ingeniería Química e Industrias Extractivas (ESIQIE), Instituto Politécnico Nacional (IPN), Zacatenco, Edificio 8 1er. Piso, 07300, Ciudad de México

[3] Escuela Nacional de Medicina y Homeopatía (ENMH), Instituto Politécnico Nacional (IPN). Av. Guillermo Massieu Helguera 239, La Escalera, Gustavo A. Madero, 07320 Ciudad de México, México

* Correspondence: mtrejov@ipn.mx

Abstract

Osteosarcoma, the most common primary malignant bone tumor in adolescents, faces treatment challenges due to metastasis and chemoresistance. This study developed a novel Au@Rh core-shell nanoparticle system functionalized with indocyanine green (ICG) to overcome hypoxia-limited photodynamic therapy (PDT). Au@Rh nanoparticles were synthesized via wet chemistry, characterized by UV-Vis spectroscopy, TEM, and cyclic voltammetry (CV). The system exhibited core-shell morphology, defined crystalline planes, photothermal conversion and electrocatalytic activity. The Au@Rh nanoparticles (109 nm total size, 90 nm Au core, 15 nm Rh shell) demonstrated dual functionality: the gold core provided photothermal conversion (7 °C temperature increase under NIR irradiation), while the rhodium shell exhibited pH-independent electrocatalytic activity for H_2O_2 decomposition, generating oxygen to alleviate tumor hypoxia. Crucially, the system showed excellent biocompatibility, with no significant cytotoxicity in both osteosarcoma (HOS) and normal osteoblast (hFOB) cells after 48-hour exposure. When activated by NIR irradiation (808 nm, 16.6 J/cm²), the complete Au@Rh-ICG system achieved selective 67% cytotoxicity in HOS cells versus only 30% in hFOB cells, demonstrating targeted therapeutic efficacy. These results position Au@Rh-ICG as a promising theranostic platform for osteosarcoma treatment, combining enhanced PDT with photothermal therapy while addressing tumor hypoxia.

Keywords: core-shell nanoparticles; cytotoxicity; osteosarcoma cells

1. Introduction

Osteosarcoma (OS), the most common primary malignant bone tumor, predominantly affects children and adolescents [1,2]. Standard treatment combines radical surgical resection with neoadjuvant and adjuvant chemotherapy. However, high recurrence rates persist due to the presence of subclinical micrometastases and the development of chemoresistance [3–6]. At diagnosis, up to 25% of cases present with detectable metastases—primarily pulmonary—which drastically reduces the 5-year survival rate from 75% in non-metastatic cases to less than 25% in metastatic disease [2].

Unlike other cancers, osteosarcoma lacks a single canonical mutation. Its oncogenesis originates from diverse genetic alterations leading to genomic instability in bone precursor cells. The main mutations identified in OS affect the tumor suppressor genes TP53 and RB1, which constitute the central oncogenic axis of this malignancy [7]. This genetic basis results in uncontrolled cellular proliferation and disorganized osteoid production, radiographically observable as a "sunburst"

 doi:10.20944/preprints202604.1292.v1

pattern [5–7]. A distinctive metabolic feature of OS is the Warburg effect, whereby tumor cells prioritize aerobic glycolysis, accumulating lactate and generating an acidic (pH ~5.0), hypoxic microenvironment with elevated H_2O_2 levels (~5 nmol/10^5 cells/h). Paradoxically, this metabolic reprogramming occurs despite the presence of functional mitochondria [8–12]. The resulting acidification of the tumor niche, in turn, promotes resistance to anoikis—a mechanism enabling cell survival upon detachment from the extracellular matrix—thereby facilitating invasion and metastasis processes [13]. Since the clinical manifestations of osteosarcoma are often ambiguous until advanced stages, therapeutic success critically depends on early diagnosis and targeted treatments, driving the continuous search for therapeutic alternatives and the identification of new molecular targets.

Photodynamic Therapy (PDT) has emerged as a promising adjuvant strategy to overcome conventional resistance in osteosarcoma [14–17]. This therapy uses photosensitizers (PS) that, when activated by light of a specific wavelength, generate reactive oxygen species (ROS) to induce cell death via oxidative stress [18]. However, the efficacy of PDT is severely limited by the hypoxic tumor microenvironment ($pO_2 \leq 2.5$ mmHg), which restricts the availability of molecular oxygen, an indispensable substrate for ROS generation [19,20].

Advances in nanotechnology offer innovative solutions to these limitations, primarily through two strategies: the development of nanocarriers that enhance the delivery and targeting of PS, and the design of bimetallic nanoparticles that simultaneously combat hypoxia while potentiating therapeutic effects. Gold nanoparticles, for example, have demonstrated potential as safe and effective nanocarriers, with the ability to induce hyperthermia when irradiated with near-infrared (NIR) light. This hyperthermia modulates the expression of heat shock proteins [21], involved in processes of differentiation, maturation, and cellular replication [22], and can enhance the immune response by increasing vascular permeability [23]. Preclinical trials in murine models have demonstrated the effectiveness of using gold as a nanocarrier for indocyanine green (ICG), a photosensitizer activatable in the NIR spectrum. The results show synergy between the PDT effect and hyperthermia ablation, as gold possesses photothermal conversion capability, absorbing infrared radiation and generating heat, thus enabling dual therapy [24]. Consistently, Li et al. (2017) demonstrated the ability of this approach to overcome PDT resistance using gold as an ICG nanocarrier [25].

Gold-rhodium core-shell (Au@Rh) structures represent the convergence of this dual approach, integrating the photothermal properties of gold with the electrocatalytic capacity of rhodium to degrade tumor H_2O_2. This catalytic activity alleviates hypoxia and, synergistically, enhances the efficacy of PDT [26]. Rhodium-based nanostructures have shown a promising profile, where synthesis with morphological control (such as nanoshells, nanoframes, and porous nanoplates) has achieved excellent biocompatibility and therapeutic efficiency in photothermal applications [27–30]. Recently, rhodium alloys have been employed as synergistic agents in osteosarcoma treatment [31], reporting encouraging results. The field of nanomedicine shows notable clinical translation, with 15 approved nanodrugs and approximately 80 candidates in 200 active clinical trials, many of which exploit passive targeting strategies mediated by the EPR (enhanced permeability and retention) effect [32–34].

In this work, we report the development and evaluation of an Au@Rh core–shell nanostructured system functionalized with indocyanine green (ICG), designed to overcome key limitations of photodynamic therapy in osteosarcoma. The Au@Rh nanoparticles (Au@Rh NPs) were successfully synthesized via soft-chemistry routes, achieving precise control over the core–shell morphology. Electrochemical characterization through cyclic voltammetry demonstrated the intrinsic capability of rhodium to decompose H_2O_2 and generate oxygen. Beyond assessing the complete Au@Rh–ICG nanoplatform, we conducted independent cytotoxicity assays using pure gold nanoparticles, free ICG, and laser-activated ICG, which allowed us to isolate the contribution of each component and confirm the synergistic effects of the multifunctional system. The nanoplatform exhibited selective cytotoxicity, achieving 67% cell death in HOS osteosarcoma cells while affecting only 30% of healthy hFOB cells, thereby validating both its therapeutic potential and selective activity. Altogether, this

 doi:10.20944/preprints202604.1292.v1

study integrates materials science, electrochemistry, and cell biology approaches to present a promising theranostic system for osteosarcoma treatment.

2. Results

2.1. Optical Properties of Au@Rh Nanoparticles

UV-Vis spectroscopy was employed to monitor nanoparticle growth due to its simplicity, reproducibility, and cost-effectiveness. The UV-Vis spectrum of the $HAuCl_4$–CTAB solution displayed absorption maxima at 232 nm and 400 nm, corresponding to d–d electronic transitions of Au(III) ions. Upon gradual addition of ascorbic acid (AA), which reduced Au(III) ions, the precursor absorption bands diminished, and a surface plasmon resonance (SPR) peak emerged at 567 nm. This peak shifted to 541 nm upon complete reduction, indicating the formation of monodisperse, near-spherical Au cores, as evidenced by the stable SPR at 541 nm (Figure 1a).

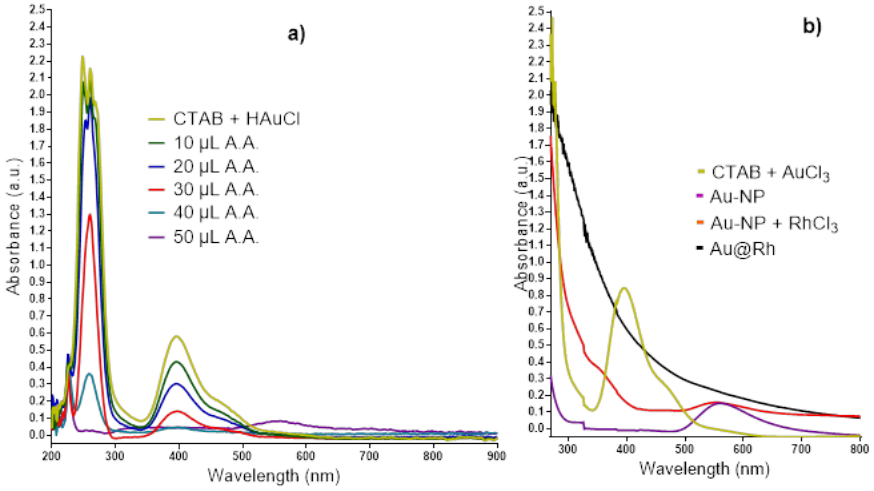

Figure 1. UV-Vis absorption profiles: (a) $HAuCl_3$-CTAB solution during ascorbic acid (AA) titration; (b) Rh shell growth stages on Au cores.

Shell growth was monitored by tracking the deposition of a Rhodium shell (Figure 1b). This was observed through the attenuation of the Au SPR signal (567 nm) following $RhCl_3$ addition. The complete quenching of the Au SPR peak after $NaBH_4$ reduction (black curve, Figure 1b) confirmed the full encapsulation of the Au cores by metallic Rh shells.

2.2. Structural Characterization of Au@Rh NPs

The High-Resolution Transmission Electron Microscopy (HRTEM) and Scanning Electron Microscopy- Energy-Dispersive X-ray Spectroscopy (SEM-EDS) analyses revealed spherical core-shell structures with Au core radius: 90 ± 5 nm (higher density Figure 2A–B), Rh shell thickness: 15 ± 2 nm (lower density, Figure 2C), average particle diameter: ± 109 nm ± 7 nm (Gaussian distribution, Figure 2D). Crystallography: Lattice fringes (Figure 2C) matched Au's (111) (d = 2.35 Å) and (002) (d = 2.04 Å) planes (JCPDS 04-0784). Elemental Composition: EDS (15 kV) detected: Au: peaks at 2.048 eV (Mα) and 9.71 keV (Kα). Rh: peaks at 0.26 eV (Mα) and 2.69 keV (Kα). Carbon tape signals were excluded (Figure 2E).

 doi:10.20944/preprints202604.1292.v1

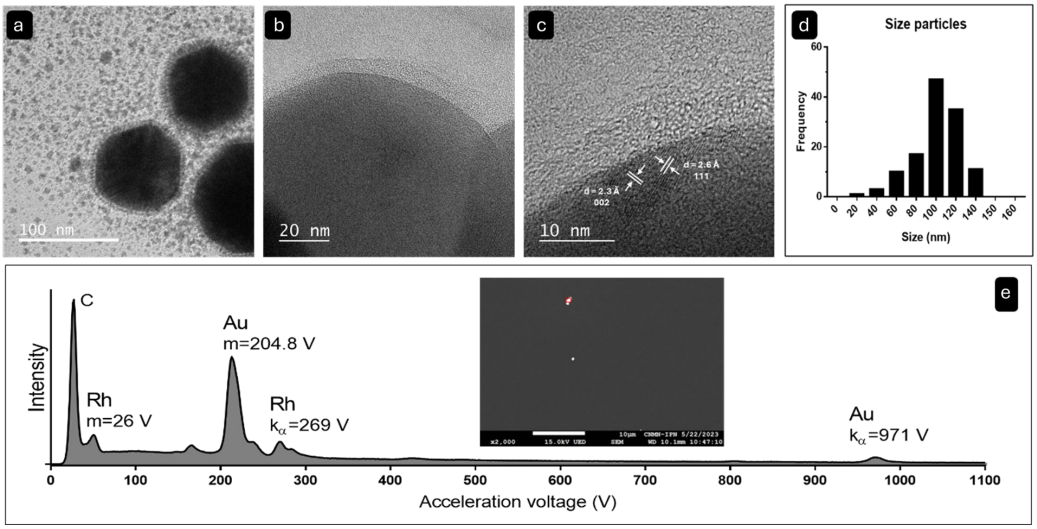

Figure 2. HRTEM/SEM-EDS of Au@Rh nanoparticles: (A) Core-shell architecture; (B) Core-shell interface; (C) Lattice spacing; (D) Size histogram; (E) EDS spectrum.

2.3. Evaluation of Electrocatalytical Activity of AuRh NPs

Cyclic voltammetry measurements performed in N_2-saturated 0.1 M KOH revealed distinct electrochemical activity. An anodic peak at −0.2 V (vs. Ag/AgCl) was observed, corresponding to hydrogen peroxide (H_2O_2) oxidation, while a cathodic peak at −0.4 V indicated oxygen (O_2) reduction (Figure 3a). The catalytic efficiency of the material was assessed by monitoring the anodic peak current density (I_p), which increased linearly with H_2O_2 concentration, yielding a correlation coefficient $R^2 > 0.98$ (Figure 3b). This relationship followed the Randles–Ševčík equation [35]:

$$I_p = 2.99 \times 10^5 \cdot \left(n(e^-)\right) \cdot \alpha^{(1/2)} \cdot A \cdot C \cdot D^{1/2} \cdot (v^{1/2})$$

Where: $n(e^-)$= electron transfer number, α = charge transfer coefficient (0.5), A = electroactive area, C = H_2O_2 concentration (mol/cm³), D = diffusion coefficient, and v = scan rate.

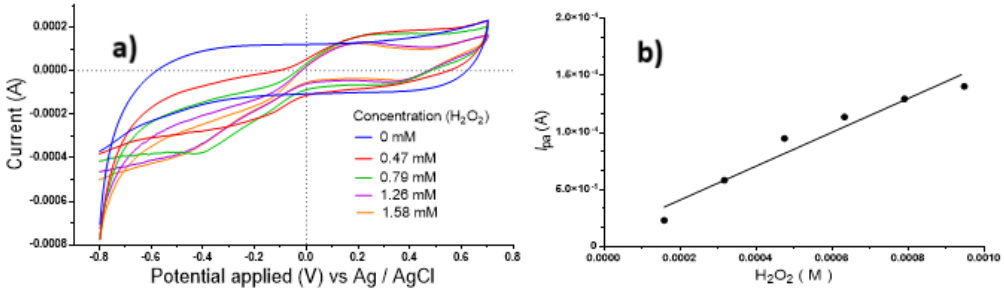

Figure 3. (a) Cyclic voltammetry of AuRh NPs with incremental H_2O_2; (b) Linear I_p vs. [H_2O_2] calibration.

Following the incorporation of indocyanine green (ICG), a transition from a quasi-reversible to an irreversible reaction was observed. This transition was indicated by the shift of the cathodic peak and the disappearance of the anodic peak once the applied potential reversed in an anodic direction. (Figure 4). This demonstrates the binding of ICG to the Au@Rh nanoparticles composed the working electrode and subsequent electron transfer, a critical phenomenon for ROS generation. Specifically, the oxygen reduction peak shifted to a less cathodic potential (E_p = −0.54 V), which is related to the formation of an Au@Rh-ICG-O_2 complex that lowers the energy required for reduction. In the anodic sweep, the absence of the peroxide-to-oxygen oxidation peak suggests an irreversible EC

 doi:10.20944/preprints202604.1292.v1

(electrochemical-chemical) process, where an electroactive species (A) is reduced to an intermediate (B), which then undergoes a homogeneous chemical reaction to form an inactive product (C):

$$A + e^- \rightleftharpoons B$$
$$B \longrightarrow C$$

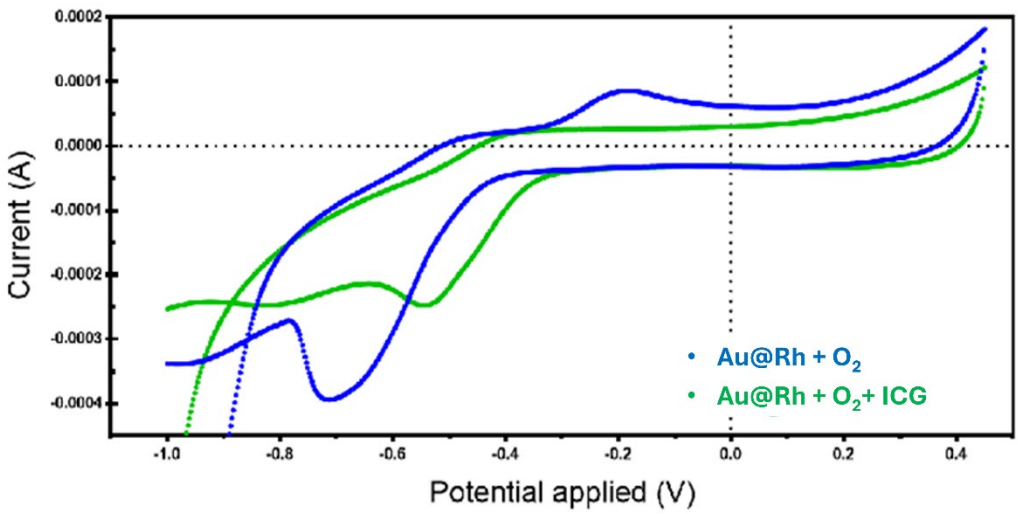

Figure 4. Cyclic voltammograms of AuRh NPs deposited on a vitreous carbon disk electrode in the absence and presence of indocyanine green (ICG), using 0.1 M phosphate buffer (pH 7.0) as the supporting electrolyte. The initial potential was −1.0 V vs. Ag/AgCl. Potential sweep rate dE/dt = 10 mV/s.

Such a case is defined as an EC reaction. It can thus be concluded that the presence of ICG within the electrolytic cell activates the Au@Rh nanoparticles, thereby promoting the complete oxidation of the hydrogen peroxide produced at the electrode-solution interface at a rate that is significantly higher than that dictated by the potential sweep conditions applied during the cyclic voltammetry tests shown in Figure 4.

2.4. Evaluation of Photothermal Conversion Efficiency

The Au@Rh NPs exhibited a linear temperature increase upon NIR irradiation, comparable to the photothermal behavior observed in pure Au NPs, thereby confirming their photothermal conversion capability. Specifically, the temperature of Au@Rh NPs increased from 24 °C to 31 °C over 10 minutes, whereas pure Au NPs achieved the same temperature rise within 5 minutes using vehicle (absolute ethanol) as control. Despite the difference in heating rates, both nanoparticle systems followed a similar linear heating trend, as illustrated in Figure 5a. Linear regression analysis yielded a correlation coefficient ($R^2 > 0.95$), further validating the consistency and reliability of the photothermal response. The thermal distribution was visualized using a heat map (Figure 5b).

3.5. Cytotoxicity Assessment in Osteosarcoma (HOS) and Osteoblast (hFOB) Cells

The effect of Au NPs on the proliferation of hFOB and HOS cells was evaluated at 0, 24, and 48 h using concentrations of 3.3 and 33.33 μg/mL. As shown in Figure 6, no significant changes in the proliferation index were observed in either hFOB or HOS cells at any of the evaluated time points following nanoparticle exposure. These findings suggest that Au NPs, at the tested concentrations, do not affect the proliferative capacity of either normal osteoblasts or osteosarcoma cells under the experimental conditions.

 doi:10.20944/preprints202604.1292.v1

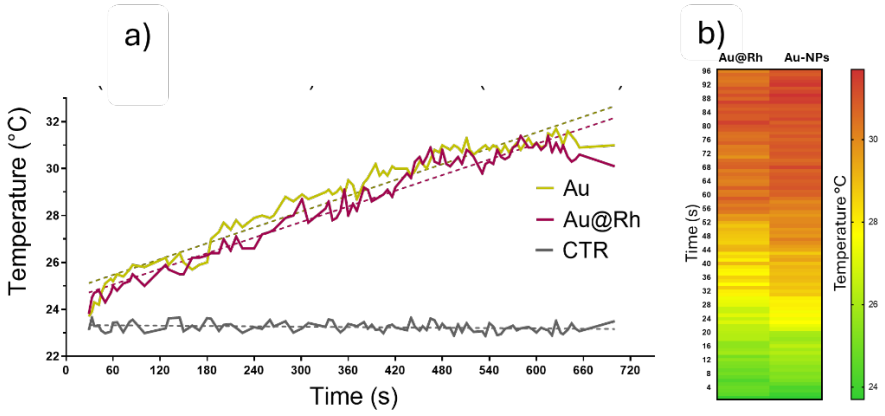

Figure 5. (a) Photothermal conversion graphic of Au@Rh NPs vs Au-NPs NIR-808 nm (16.67 J/cm²); (b) Heat map of photothermal conversion. CTR represents the control measurement obtained from the glass slide that was used as the sample support substrate.

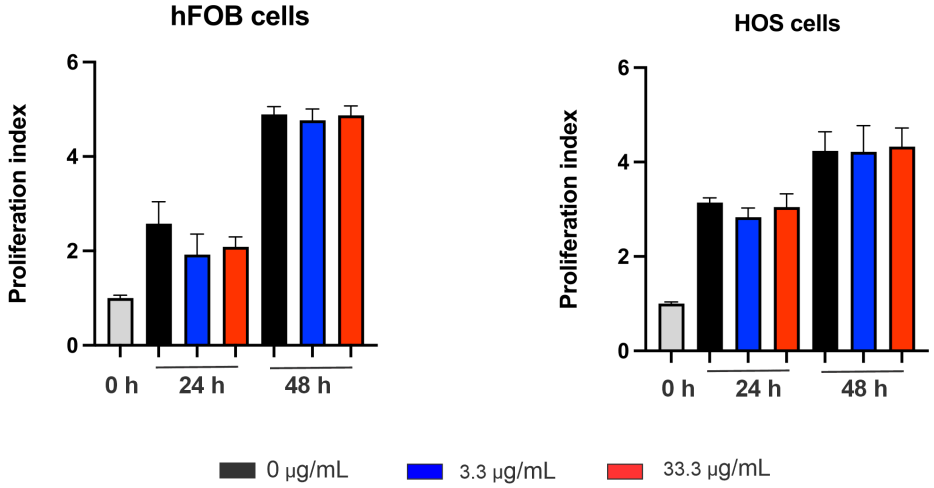

Figure 6. Relative proliferation index of hFOB and HOS cells exposed to AuNPs (3.3 and 33.33 µg/mL) for 24 and 48 h, as determined by the MTT assay. Data are presented as mean ± SEM (n = 3 independent experiments). Statistical analysis was performed using one-way ANOVA followed by Tukey's multiple comparison test. No statistically significant differences were observed compared to the control.

The effect of core–shell nanoparticles (Au@Rh) on the proliferation of hFOB and HOS cells was evaluated at 24 and 48 h. Consistent with the results observed for AuNPs, no significant changes in the proliferation index were detected in either cell line following exposure to Au@Rh nanoparticles compared to the untreated control (Figure 7). The proliferation index remained stable across all treatment groups and time points, suggesting that the core–shell nanostructure does not affect the proliferative capacity of either normal osteoblasts or osteosarcoma cells under the experimental conditions.

Independent cytotoxicity assays of the photosensitizer ICG were performed. As shown in Figure 8, ICG alone did not induce significant cytotoxicity in HOS or hFOB cells after 24 or 48 hours of incubation at 3.3 µg/mL compared with the untreated control. In contrast, at a ten-fold higher concentration (33.33 µg/mL), a slight cytotoxic effect was observed. It is noteworthy that ICG is a clinically relevant agent approved by the U.S. FDA for use in medical applications for many years, which supports its favorable safety profile.

 doi:10.20944/preprints202604.1292.v1

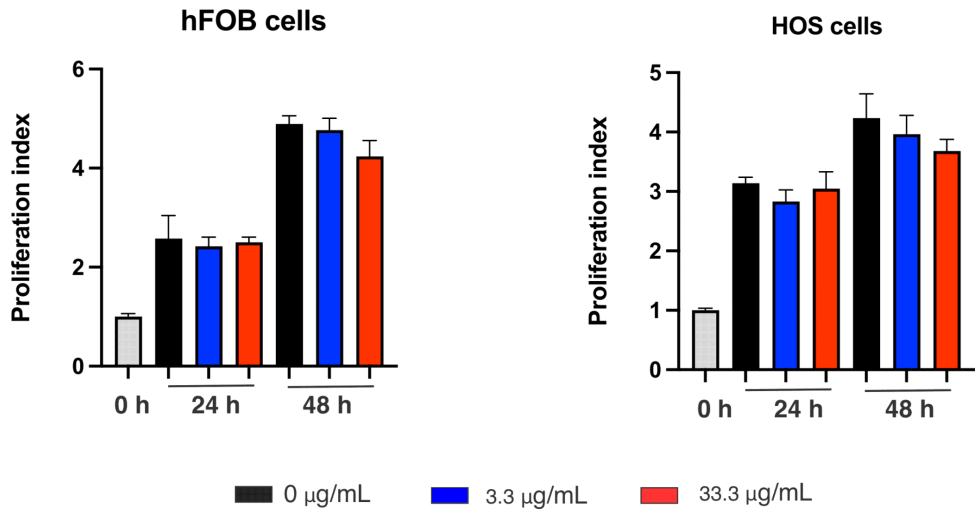

Figure 7. Relative proliferation index of hFOB and HOS cells exposed to Au@Rh core–shell nanoparticles at 24 and 48 h, as determined by the MTT assay. Data are presented as mean ± SD (n = 3 independent experiments). Statistical analysis was performed using one-way ANOVA followed by Tukey's multiple comparison test. No statistically significant differences were observed compared to the control.

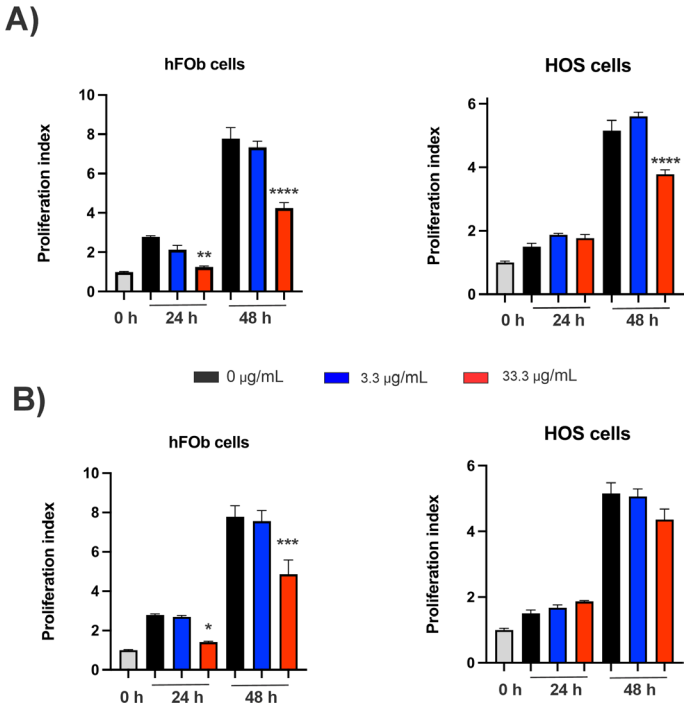

Figure 8. Relative proliferation index of hFOB and HOS cells exposed to (A) free ICG and (B) Au@Rh–ICG nanoparticles at 24 and 48 h, as determined by the MTT assay. ICG was evaluated at 3.3 and 33.33 µg/mL. Data are presented as mean ± SD (n = 3 independent experiments). Statistical analysis was performed using one-way ANOVA followed by Tukey's multiple comparison test. Statistically significant differences compared to the control are indicated (*p < 0.05, **p < 0.01, ***p < 0.001, ****p < 0.0001).

The effect of free ICG and Au@Rh–ICG nanoparticles on the proliferation of hFOB and HOS cells was evaluated at 24 and 48 h. As shown in Figure 8A, treatment with free ICG at 3.3 µg/mL did not induce significant changes in the proliferation index in either cell line compared to the untreated control. However, at 33.33 µg/mL, a slight but statistically significant decrease in the proliferation index was observed, indicating a mild concentration-dependent effect that becomes evident only at higher concentrations.

 doi:10.20944/preprints202604.1292.v1

In contrast, cells treated with Au@Rh–ICG nanoparticles Figure 8B exhibited a more pronounced reduction in the proliferation index; however, this effect was primarily observed at the highest concentration and longer exposure times. This effect was more evident in hFOB cells, suggesting an enhanced impact of the nanoparticle–photosensitizer system compared to free ICG under these conditions. Overall, these results indicate that conjugation of ICG to Au@Rh nanoparticles potentiates its biological effect, particularly at elevated concentrations, leading to a greater decrease in cell proliferation.

Figure 9 illustrates the relative proliferation index of hFOB and HOS cells following treatment with Au@Rh–ICG nanoparticles under dark conditions and after near-infrared (NIR) irradiation. Under dark conditions, the nanoparticles did not significantly affect cell proliferation at either 24 or 48 h, confirming their cytocompatibility in the absence of external stimulation. In contrast, exposure to NIR irradiation (808 nm) resulted in a significant reduction in the proliferation index, particularly at 48 h. This effect was more pronounced in HOS osteosarcoma cells than in hFOB osteoblasts, indicating a higher susceptibility of tumor cells to the photothermal treatment.

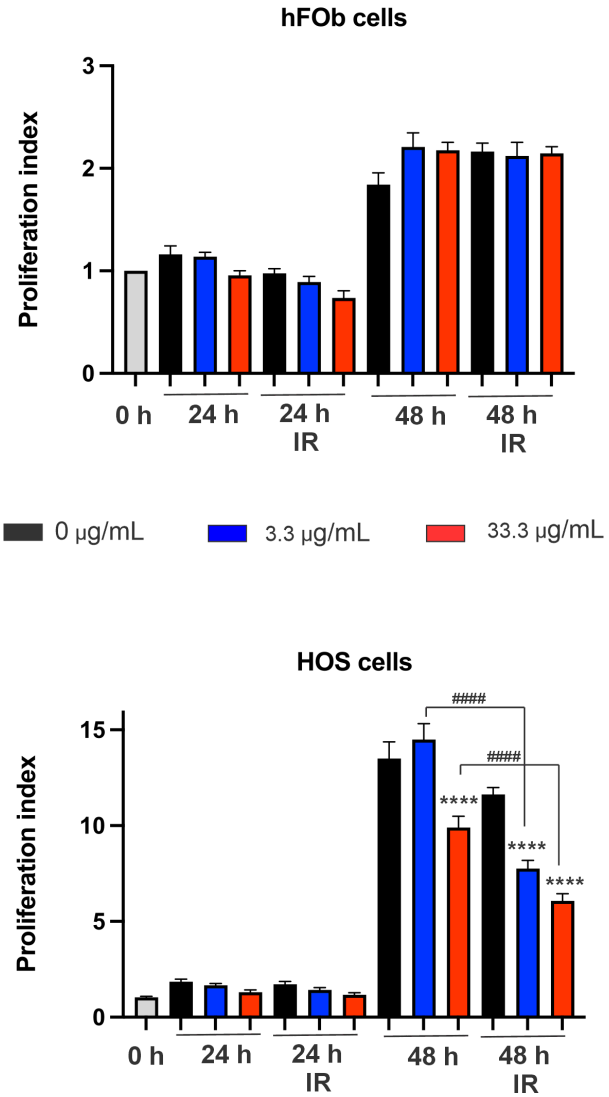

Figure 9. Relative proliferation index of hFOB and HOS cells treated with Au@Rh–ICG nanoparticles under dark conditions and upon near-infrared (808 nm) irradiation at 1 W for 10 min (20 J/cm²) at 24 and 48 h post-treatment. Cell proliferation was evaluated by the MTT assay. Statistical analysis was performed using one-way ANOVA followed by Tukey's multiple comparison test. Significant differences are indicated as follows: ****$p < 0.0001$ vs control and ####$p < 0.0001$ vs non-irradiated cells.

 doi:10.20944/preprints202604.1292.v1

3. Discussion

The synthesis of gold nanoparticles via ascorbic acid (AA)-mediated reduction of $AuCl_4^-$ is well-established, with AA facilitating electron transfer to reduce Au(III) to Au(0) through intermediate complexation [30]. In our system, CTAB plays a dual role: (1) as a surfactant stabilizing nascent Au nuclei via electrostatic interactions between CTA^+ cations and $AuCl_4^-$ anions (forming $[CTA]^+$-$[AuCl_4]^-$ complexes), and (2) as a structure-directing agent modulating nanoparticle growth kinetics through sub-/post-micellar effects [30]. UV-Vis spectroscopy confirmed the reduction process, marked by the disappearance of Au(III) d-orbital transitions (232 nm and 327 nm) and the emergence of a surface plasmon resonance (SPR) peak at 541 nm, characteristic of spherical Au cores (Figure 1a). The quenching of this SPR signal during Rh shell deposition (Figure 1b) aligns with prior reports of core-shell formation, where metallic shells attenuate plasmonic responses [27].

HRTEM analysis revealed polycrystalline Au cores with dominant (111) and (002) facets (JCPDS 04-0784), consistent with the fcc structure of gold (Figure 2C). The amorphous Rh shell (15 ± 2 nm thickness) lacked discernible lattice fringes, likely due to rapid $NaBH_4$-driven reduction inhibiting atomic ordering—a phenomenon observed in other wet-chemical Rh nanostructure syntheses [29]. Spatially resolved EDS mapping confirmed the core-shell architecture, with distinct Au (Mα/Kα) and Rh (Mα/Kα) signals (Figure 2E).

3.1. Electrocatalytic Properties

The Rh shell exhibited pH-independent electrocatalytic activity for H_2O_2 decomposition, as demonstrated by cyclic voltammetry (CV) (Figs 3a, 4). The linear relationship between anodic current density (I_p) and H_2O_2 concentration ($R^2 > 0.98$) follows the Randles-Sevcik equation, indicating diffusion-controlled kinetics [35]. ICG binding to the Au@Rh nanoparticles on the working electrode is evidenced by the shift in the half-wave potential from O_2 to H_2O_2 (Figure 4) This demonstrates that spacer molecules or biconjugates anchored to the surface of the metal nanoparticles are not required. Additionally, the integration of ICG within the nanoparticle structure serves to initiate the decomposition of the hydrogen peroxide that is produced at the electrode-solution interface.

3.2. Cytocompatibility and Therapeutic Implications

The physicochemical properties of gold nanoparticles (AuNPs), particularly their size and shape, play a critical role in determining their cytotoxicity. Previous studies have shown that spherical AuNPs within the 6–22 nm range do not compromise the viability of hFOB or MG-63 cells [36]. In contrast, the nanoparticles synthesized in this study were larger (~90 nm); however, no significant cytotoxic effects were observed in hFOB or HOS cells after 48 h of exposure. These findings suggest that spherical AuNPs can retain their biocompatibility even at larger sizes, indicating that size alone may not be the sole determinant of cytotoxicity. Furthermore, Au@Rh nanostructures exhibited a favorable cytocompatibility profile, with no significant reduction in cell viability at the tested concentration. This behavior may be attributed to the formation of a RhOx surface layer under physiological condi-tions, which could enhance biocompatibility, while the metallic Rh core preserves its catalytic properties.

To further enhance functionality, Au@Rh nanoparticles were integrated with indocya-nine green (ICG), a compound originally developed as a dye and later approved by the FDA as a contrast agent for microsurgical procedures and as a photosensitizer, thereby generating a multifunctional platform. In our study, ICG alone did not induce cytotoxic effects in HOS or hFOB cells after 24–48 h at a concentration of 3.3 μg/mL; however, higher concentrations resulted in decreased cell viability. These findings are con-sistent with prvious reports indicating that ICG concentrations below 15 μg/mL are generally well toleated by osteoblasts [37] and MG-63 osteosarcoma cells [38].

Importantly, the absence of cytotoxic effects under dark conditions, together with the significant reduction in cell proliferation upon NIR irradiation, highlights the controlled and stimulus-responsive behavior of the Au@Rh–ICG system. The enhanced sensitivity of HOS osteosarcoma cells

 doi:10.20944/preprints202604.1292.v1

compared to non-tumoral hFOB cells suggests a degree of selectivity that is highly desirable for therapeutic applications. This selectivity may be associated with the reduced capacity of cancer cells to manage oxidative stress and hyperthermia-induced damage, as well as their altered redox homeostasis. Although similar phototherapeutic effects have been reported in other cancer models, such as breast cancer [39], it is important to consider the intrinsic biological differences between tumor types. Osteosarcoma arises from mesenchymal tissue, whereas breast cancer is of epithelial origin, involving distinct signaling pathways and tumor micro-environment characteristics. In this context, the differential response observed here may be further influenced by the unique metabolic features of osteosarcoma cells, in-cluding their redox imbalance and susceptibility to oxidative stress, which can poten-tiate both photothermal and photodynamic effects.

Overall, these findings support the potential of the Au@Rh–ICG nanoplatform as a bi-ocompatible and effective system for NIR-triggered phototherapy, particularly in the context of osteosarcoma treatment. In addition, the results highlight the promise of rhodium-based nanomaterials in catalytic nanomedicine applications [29], where their intrinsic catalytic activity may further enhance therapeutic outcomes.

Nevertheless, despite these encouraging results, additional studies are required to bet-ter understand nanoparticle penetration, distribution, and retention within the dense extracellular matrix characteristic of osteosarcoma tumors. These aspects are critical for optimizing therapeutic efficacy in vivo.

Taken together, the Au@Rh–ICG nanosystem represents a significant step forward in the development of multifunctional nanoplatforms for the treatment of hypoxic and metabolically complex tumors, providing a promising strategy for improving the ef-fectiveness of phototherapy in osteosarcoma.controlled drug release, and improve photoacoustic imaging performance [26].

4. Materials and Methods

4.1. Synthesis of Au@Rh Core-Shell Nanoparticles

Metal nanoparticle synthesis was performed using hydrogen tetrachloroaurate(III) hydrate ($HAuCl_4 \bullet xH_2O$, Sigma-Aldrich-520918) and rhodium(III) chloride hydrate ($RhCl_3 \bullet xH_2O$, Sigma-Aldrich-520772) as ionic precursors, with ascorbic acid (Merck) and sodium borohydride ($NaBH_4$, Fluka-71321) as reducing agents. Cetyltrimethylammonium bromide (CTAB, Sigma-Aldrich-H5882) served as the surfactant. All reagents were used as received, without further purification. Seed Formation: 8 mL of 100 mM CTAB solution was heated to 60 °C in a water bath. Under vigorous magnetic stirring (500 rpm), 250 µL of 10 mM $HAuCl_4$ was added, followed by 200 µL of 80 mM ascorbic acid, inducing a pink coloration (Au core formation). Shell Deposition: 850 µL of 10 mM $RhCl_3$ was introduced, with continuous stirring for 5 min. Then, 400 µL of 100 mM $NaBH_4$ was added to initiate Rh shell growth, evidenced by a color shift to dark gray. Purification: Particles were washed with ethanol (1:1 v/v), centrifuged (15,000 ×g, 10 min), and redispersed via ultrasonication (30 s, 40 kHz). This wash cycle was repeated twice, and the final product was suspended in 1 mL of absolute ethanol and stored at 4 °C.

4.2. Spectroscopic Characterization of Au@Rh Core-Shell Nanoparticles

UV-Vis spectra (400–800 nm) were acquired using a PerkinElmer XLS spectrophotometer to monitor plasmon resonance shifts during Au core growth. Morphological Analysis was conducted on a JEOL JSM 7800F microscope (15 kV, secondary/backscattered electron detection). Atomic-Resolution TEM was performed on a JEOL JEM-ARM 200CF (20 kV) with EDS for elemental mapping.

4.3. Photothermal Conversion: Experimental Setup

 doi:10.20944/preprints202604.1292.v1

Photothermal measurements were performed using a portable infrared (IR) camera (Model HTI-19, HT Instruments, China) with the following specifications: Spectral range: 8–14 μm (far-infrared band). Thermal resolution: ≤0.1 °C (at 30 °C). Accuracy: ±2 °C or ±2% of reading (whichever is greater). Field of view (FOV): 25° × 19° with a distance-to-spot ratio (D:S) of 10:1. Temperature range: −20 °C to +400 °C (extendable to +1000 °C with an optional filter). Sensitivity (NETD): <50 mK. Refresh rate: 9 Hz. Adjustable emissivity: 0.1–1.0 (pre-calibrated for metallic surfaces and aqueous media).

Sample preparation: An ethanol suspension of nanoparticles was deposited on a glass slide to achieve a uniform distribution of 100 μg Au@Rh over an area of 0.196 cm^2 (equivalent to a 0.5 cm diameter spot). The samples were dried in a vacuum oven at 60 °C for 60 minutes. An identical protocol was applied to pure gold nanoparticles (Au NPs), synthesized under the same conditions but without the rhodium shell.

Irradiation: Samples were exposed to an 808 nm near-infrared (NIR) laser at 1 W power, delivering a fluence of 16.67 J/cm^2 over a 10-minute period. Temperature changes were recorded with a temporal resolution of 3-second intervals.

Environmental control: All experiments were conducted at 23 °C and 50% relative humidity inside a laminar flow chamber to minimize thermal drift and ensure consistent experimental conditions. Absolute ethanol was used as a control in both cases.

4.4. Electrochemical Characterization

Electrocatalytic activity was evaluated using cyclic voltammetry (CV) on a Metrohm Autolab 302N potentiostat. Working electrode: Glassy carbon modified with Au@Rh ink prepared by mixing 10 μL of nanoparticle suspension, 250 μL isopropanol, and 10 μL of Nafion, followed by sonication 3 minutes. Reference electrode: Ag/AgCl (3 M KCl). Counter electrode: Pt wire. Parameters: Scan range: +0.8 to −0.7 V vs. Ag/AgCl; electrolyte: pH 7.4 phosphate buffer.

For FRA impedance analysis at OCP, a DRP-C110 screen-printed carbon electrode was used (working and counter electrodes: carbon; reference electrode: silver). The electrolyte was phosphate-buffered saline pH 7.4.

4.5. Formation of the Nanostructured System Au@Rh-ICG

Indocyanine green (ICG) was used as the photosensitizing agent. Prior to use, the vial was subjected to a drying process at 50 °C for 60 minutes. Subsequently, 1 mg of the dried compound was transferred into a microtube and resuspended in 1 mL of a dimethyl sulfoxide/deionized water mixture (1:4). The ICG solution was prepared immediately before use, as storage in solution is not feasible due to dimer formation, precipitation, and alterations in its optical properties. To facilitate integration with the metallic nanostructures, 5 mg of Au@Rh core–shell nanoparticles were added to the ICG solution. The mixture was stirred at room temperature for 60 minutes and then centrifuged at 13,000 ×g for 5 minutes. The supernatant was discarded, and 0.5 mL of absolute etanol was added to the pellet, followed by 5 minutes of sonication. This washing step was repeated until no residual ICG remained. The resulting nanocomposite, suspended in saline solution (0.9% NaCl, PISA Laboratory), was dispensed into pre-weighed microtubes in 50 μL aliquots. The suspension mass was recorded, after which the material was dried at 50 °C for 3 hours under vacuum. The final weight of each microtube containing the dried material was used to determine the mass corresponding to 50 μL of suspension, enabling calculation of the concentration of the Au@Rh–ICG nanocomposite.

4.7. Cytotoxicity Assessment in hFOB and HOS Cells

The human osteoblast cell line hFOB1.19 (CRL-3602) and human osteosarcoma cell line HOS (CRL-1543) were acquired from the American Type Culture Collection (ATCC Manassas, VA, USA) and cultured in Eagle Minimum Essential Medium (12800-058 GIBCO, Auckland NZ) supplemented with 10% fetal bovine serum (FBS) (S1560-500 Biowest, Riverside, MO, USA) and 1% penicillin-streptomycin (15240-062 GIBCO, NY, USA) in a humidified incubator at 37 °C and 5% CO_2. Once the

 doi:10.20944/preprints202604.1292.v1

cells reached a confluency of about 80%, they were trypsinized and were seeded in 96-well plates at a density of 5×10^3 cells/well and incubated for 24 h. Cells were treated with Au, Au@Rh and Au@Rh-ICG nanoparticles at concentrations of 3.33, or 33.33 μg/mL in fresh medium and incubated for 0, 24, or 48 hours. After incubation, the medium was replaced with 200 μL MTT solution (5 mg/mL in culture medium). Following 3 hours incubation period, the resulting formazan crystals were dissolved by adding 200 μL of DMSO per well, with gentle agitation for 5 min. Absorbance was measured at 570 nm (signal) and 660 nm (reference) using a Biotek Epoch microplate reader. Untreated cells served as positive controls, and blank wells for background correction. All experiments were conducted in triplicate.

4.8. Photosensitiser Activation

Two 96-well plates were prepared under the conditions described, divided into three groups (0, 3.3, 33.33 μg/mL of Au@Rh-ICG). A subgroup of each concentration was irradiated with an 808 nm NIR laser (1 W, fluence 16.67 J/cm²) for a period of 10 minutes. After this, the MTT assay was conducted after a period of 24 hours to Au@Rh-ICG and 24, 48 hours to pure ICG.

5. Conclusions

A multifunctional Au@Rh core–shell nanoplatform functionalized with indocyanine green (ICG) was successfully developed and evaluated as a theranostic strategy for osteosarcoma. The system combines the photothermal properties of gold with the electrocatalytic activity of rhodium, enabling hydrogen peroxide decomposition and local oxygen generation to mitigate tumor hypoxia.

Electrochemical characterization confirmed the catalytic role of the rhodium shell, while photothermal assays demonstrated efficient near-infrared light–to-heat conversion. Cytotoxicity studies showed that AuNPs, Au@Rh nanoparticles, and free ICG were biocompatible in both HOS osteosarcoma and hFOB osteoblast cells. Importantly, upon NIR irradiation, the complete Au@Rh–ICG system induced a selective photodynamic effect, achieving up to 67% cytotoxicity in HOS cells while preserving higher viability in normal osteoblasts.

Overall, these results highlight the potential of Au@Rh–ICG nanoparticles as a multifunctional platform that integrates catalysis, photothermal conversion, and photodynamic activity, offering a promising approach to overcome hypoxia-related limitations in osteosarcoma therapy.

Supplementary Materials: The following supporting information can be downloaded at the website of this paper posted on Preprints.org.

Author Contributions: Sergio Zamudio: Experimental and Writing—original draft. Martin Trejo: My responsibilities include research into nanoparticle, supervision, and writing—review and editing. María Elena Manríquez: Materials Research and Writing. Nury Perez and Ángel Bañuelos: The project involved research, writing and review of the final paper version on osteoblast cell research.

Funding: The results presented in this article were supported by the Instituto Politécnico Nacional (IPN) through the Office of Research and Graduate Studies (SIP) as part of the Multidisciplinary Project SIP 2241.

Institutional Review Board Statement: Informed Consent Statement: Not applicable. This study did not involve humans or animals.

Data Availability Statement: The data presented in this study are available in the article and supplementary material. Raw data are available from the corresponding author upon reasonable request.

Acknowledgments: The authors thank the Instituto Politécnico Nacional (IPN) for support provided.

Conflicts of Interest: The authors declare no conflicts of interest.

 doi:10.20944/preprints202604.1292.v1

Abbreviations

The following abbreviations are used in this manuscript: **OS**: Osteosarcoma; **PDT**: Photodynamic Therapy; **PS**: Photosensitizer; **ROS**: Reactive Oxygen Species; **NIR**: Near-Infrared; **NPs**: Nanoparticles; **AuNPs**: Gold Nanoparticles; **Au@Rh**: Gold-Rhodium Core-Shell Nanoparticles; **ICG**: Indocyanine Green; **Au@Rh-ICG**: Gold-Rhodium Core-Shell Nanoparticles functionalized with Indocyanine Green; **HOS**: Human Osteosarcoma Cell Line (ATCC® CRL-1543™); **hFOB**: Human Fetal Osteoblast Cell Line (ATCC® CRL-11372™); **EPR**: Enhanced Permeability and Retention Effect; **CV**: Cyclic Voltammetry; **SPR**: Surface Plasmon Resonance; **HRTEM**: High-Resolution Transmission Electron Microscopy; **SEM-EDS**: Scanning Electron Microscopy with Energy-Dispersive X-ray Spectroscopy; **MTT**: 3-(4,5-Dimethylthiazol-2-yl)-2,5-diphenyltetrazolium bromide assay.

References

1. Beird HC, Bielack SS, Flanagan AM, Gill J, Heymann D, Janeway KA, Livingston JA, Roberts RD, Strauss SJ, Gorlick R. Osteosarcoma. Nat Rev Dis Primers 2022, *8*, 77. doi: 10.1038/s41572-022-00409-y.
2. Nyeko R, Geriga F, Angom R, Kambugu JB, van Heerden J. The management of osteosarcoma in children and adolescents in a resource-limited setting: quality improvement considerations to improve treatment outcomes. BMC Cancer. 2024 *24*. 1061. doi: 10.1186/s12885-024-12786-6.
3. Tsuda Y, Tsoi K, Parry MC, Stevenson JD, Fujiwara T, Sumathi V, Jeys LM. Impact of chemotherapy-induced necrosis on event-free and overall survival after preoperative MAP chemotherapy in patients with primary high-grade localized osteosarcoma. Bone Joint J. 2020, *102-B(6)*, 795-803. doi: 10.1302/0301-620X.102B6.BJJ-2019-1307.R1.
4. Jeys LM, Thorne CJ, Parry M, Gaston CL, Sumathi VP, Grimer JR. A Novel System for the Surgical Staging of Primary High-grade Osteosarcoma: The Birmingham Classification. Clin Orthop Relat Res. 2017 475(3) 842-850. doi: 10.1007/s11999-016-4851-y.
5. Xu J, Xie L, Guo W. Neoadjuvant Chemotherapy Followed by Delayed Surgery: Is it Necessary for All Patients With Nonmetastatic High-Grade Pelvic Osteosarcoma? Clin Orthop Relat Res. 2018 476(11). 2177-2186. doi: 10.1097/CORR.0000000000000387.
6. Bajpai J, et al. Outcomes in non-metastatic treatment naive extremity osteosarcoma patients treated with a novel non-high dosemethotrexate-based, dose-dense combination chemotherapy regimen 'OGS-12'. Eur J Cancer. 2017 *85*. 49-58. doi: 10.1016/j.ejca.2017.08.013.
7. Chen, X., Bahrami, A., Pappo, A., et al. Recurrent Somatic Structural Variations Contribute to Tumorigenesis in Pediatric Osteosarcoma. Cell Reports 2014, *7*(1), 104-112. https://doi.org/10.1016/j.celrep.2014.03.003
8. Jaworska M, et al. The Warburg effect: a score for many instruments in the concert of cancer and cancer niche cells. Pharmacol Rep. 2023, 75(4). 876-890. doi: 10.1007/s43440-023-00504-1.
9. Potter M, Newport E, Morten KJ. The Warburg effect: 80 years on. Biochem Soc Trans. 2016, *44*. 1499-1505. doi: 10.1042/BST20160094.
10. Lu J, Tan M, Cai Q. The Warburg effect in tumor progression: mitochondrial oxidative metabolism as an anti-metastasis mechanism. Cancer Lett. 2015, 356(2 Pt A). 156-64. doi: 10.1016/j.canlet.2014.04.001.
11. Vaupel P, Schmidberger H, Mayer A. The Warburg effect: essential part of metabolic reprogramming and central contributor to cancer progression. Int J Radiat Biol. 2019, 95(7). 912-919. doi: 10.1080/09553002.2019.1589653.
12. Kobayashi Y, et al. Warburg effect in Gynecologic cancers. J Obstet Gynaecol Res. 2019, 45(3). 542-548. doi: 10.1111/jog.13867.
13. Czarnecka AM, et al. Molecular Biology of Osteosarcoma. Cancers 2020, *12*(8), 2130. https://doi.org/10.3390/cancers12082130
14. Li, G., Wang, C., Jin, B. et al. Advances in smart nanotechnology-supported photodynamic therapy for cancer. Cell Death Discov. 10, 466 (2024). https://doi.org/10.1038/s41420-024-02236-4
15. Yujia Xin, et. al., Nanodynamic therapies for osteosarcoma: Recent advances and future perspectives, Chemical Engineering Journal 2026, 527, 171582, https://doi.org/10.1016/j.cej.2025.171582

 doi:10.20944/preprints202604.1292.v1

16. Yang J. et. al., Progress of phototherapy for osteosarcoma and application prospect of blue light photobiomodulation therapy, Front. Oncol. 2022, 12:1022973. doi: 10.3389/fonc.2022.1022973
17. Khaled Al Jarrah, et. al., A Novel Approach for Enhanced Osteosarcoma Photodynamic Therapy Using Encapsulated Methylene Blue in Silica Nanoparticles, J. Compos. Sci. 2023, 7(4), 137; https://doi.org/10.3390/jcs7040137
18. Volsi, A. L., Scialabba, C., Vetri, V., Cavallaro, G., Licciardi, M., & Giammona, G. Near-Infrared Light Responsive Folate Targeted Gold Nanorods for Combined Photothermal-Chemotherapy of Osteosarcoma. ACS Appl Mater Interfaces 2017, *9*(16), 14453-14469. https://doi.org/10.1021/acsami.7b03711
19. Liang Hong, et al., Recent Advances in Strategies for Addressing Hypoxia in Tumor Photodynamic Therapy, Biomolecules 2022, 12(1), 81; https://doi.org/10.3390/biom12010081
20. Yihenew Simegniew Birhan, et. al., Oxygen tension regulating nanoformulation for the improved photodynamic therapy of hypoxic tumors, Materials Today Bio, 2025, 31, 101587, https://doi.org/10.1016/j.mtbio.2025.101587
21. Khojastehnezhad, M. A., Seyedi, S. M. R., Raoufi, F., & Asoodeh, A. Association of hypoxia-inducible factor 1 expressions with prognosis role as a survival prognostic biomarker in the patients with osteosarcoma: a meta-analysis. Expert Rev Mol Diagn 2022, *22*(12), 1099-1106. https://doi.org/10.1080/14737159.2022.2157719
22. Luo, D., Ren, H., Zhang, W., Xian, H., Lian, K., & Liu, H. Clinicopathological and prognostic value of hypoxia-inducible factor-1α in patients with bone tumor: a systematic review and meta-analysis. J Orthop Surg Res 2019, *14*(1), 56. https://doi.org/10.1186/s13018-019-1101-5
23. Clever, D., Roychoudhuri, R., Constantinides, M. G., et al. Oxygen Sensing by T Cells Establishes an Immunologically Tolerant Metastatic Niche. Cell 2016, *166*(5), 1117-1131.e14. https://doi.org/10.1016/j.cell.2016.07.032
24. Shirata, C., Kaneko, J., Inagaki, Y., et al. Near-infrared photothermal/photodynamic therapy with indocyanine green induces apoptosis of hepatocellular carcinoma cells through oxidative stress. Sci Rep 2017, *7*(1), 13958. https://doi.org/10.1038/s41598-017-14401-0
25. Li, W., Guo, X., Kong, F., et al. Overcoming photodynamic resistance and tumor targeting dual-therapy mediated by indocyanine green conjugated gold nanospheres. J Control Release 2017, *258*, 171-181. https://doi.org/10.1016/j.jconrel.2017.05.015
26. Wang J, et al. A Porous Au@Rh Bimetallic Core-Shell Nanostructure as an H_2O_2-Driven Oxygenerator to Alleviate Tumor Hypoxia for Simultaneous Bimodal Imaging and Enhanced Photodynamic Therapy. Adv Mater 2020, *32*(22), e2001862. doi: 10.1002/adma.202001862.
27. Kang, Y., Xue, Q., Peng, R., Jin, P., Zeng, J., Jiang, J., & Chen, Y. Bimetallic AuRh nanodendrites consisting of Au icosahedron cores and atomically ultrathin Rh nanoplate shells: synthesis and light-enhanced catalytic activity. NPG Asia Mater 2017, *9*(7), e407. https://doi.org/10.1038/am.2017.114
28. Machuca A, et al. Rhodium Nanoparticles as a Novel Photosensitizing Agent in Photodynamic Therapy against Cancer. Chemistry 2020, *26*(34), 7685-7691. doi: 10.1002/chem.202001112.
29. Kang S, et al. Morphology-Controlled Synthesis of Rhodium Nanoparticles for Cancer Phototherapy. ACS Nano 2018 *12*(7), 6997-7008. doi: 10.1021/acsnano.8b02698.
30. Khan, Z., Singh, T., Hussain, J. I., & Hashmi, A. A. Au(III)–CTAB reduction by ascorbic acid: Preparation and characterization of gold nanoparticles. Colloids Surf B Biointerfaces 2012, *104*, 11-17. https://doi.org/10.1016/j.colsurfb.2012.11.017
31. Liang, Y., Liao, C., Guo, X., et al. RhRu Alloy-Anchored MXene Nanozyme for Synergistic Osteosarcoma Therapy. Small 2023, *19*(22), e2205511. https://doi.org/10.1002/smll.202205511
32. García Calavia P, et al. Photosensitiser-gold nanoparticle conjugates for photodynamic therapy of cancer. Photochem Photobiol Sci 2018, *17*(11), 1534-1552. doi: 10.1039/c8pp00271a.
33. Fan, D., et al. Nanomedicine in cancer therapy. Sig Transduct Target Ther 2023, *8*, 293. https://doi.org/10.1038/s41392-023-01536-y
34. Gomerdinger, V.F., Nabar, N. & Hammond, P.T. Advancing engineering design strategies for targeted cancer nanomedicine. Nat Rev Cancer 2025, *25*, 657--683. https://doi.org/10.1038/s41568-025-00847-2

 doi:10.20944/preprints202604.1292.v1

35. Compton, R.G., Banks, C.E. Understanding Voltammetry, 3rd ed.; World Scientific: New Jersey, 2018; p. 312.
36. P. Suchomel, K. P. Stulajterova, E. B. Sedenkova, et al., Impact of gold nanoparticles shape on their cytotoxicity against human osteoblast and osteosarcoma in in vitro model. Evaluation of the safety of use and anti-cancer potential, Journal of Materials Science: Materials in Medicine, 2019, 30:22 https://doi.org/10.1007/s10856-019-6221-2
37. Solarte, D.L.G.; Rau, S.J.; Hellwig, E.; Vach, K.; Al-Ahmad, A. Antimicrobial Behavior and Cytotoxicity of Indocyanine Green in Combination with Visible Light and Water-Filtered Infrared A Radiation against Periodontal Bacteria and Subgingival Biofilm. Biomedicines 2022, 10, 956. https://doi.org/10.3390/biomedicines10050956
38. Aghayan, S., et al. Evaluation of Indocyanine-Mediated Photodynamic Therapy Cytotoxicity in Human Osteoblast-Like Cells: an In Vitro Study, Folia Medica, 2022, 64(6), 932-938. DOI: 10.3897/folmed.64.e67475
39. Wang, Y., Zhang, L., Zhao, G. et al. Homologous targeting nanoparticles for enhanced PDT against osteosarcoma HOS cells and the related molecular mechanisms. J Nanobiotechnol 20, 83 (2022). https://doi.org/10.1186/s12951-021-01201-y